Chapter 3

Flavour phenomenology of the flavon of the $\mathscr{Z}_N \times \mathscr{Z}_M$ flavour symmetries

In the conventional FN mechanism based on $U(1)_F$ flavour symmetry, the VEV of the flavon field χ breaks the $U(1)_F$ flavour symmetry spontaneously. The scale Λ, where the higher dimension operators get renormalized, is not predicted by the FN mechanism, and it can be anywhere between the weak and the Planck scale. The essential requirement for the FN mechanism is that the flavour symmetry is broken weakly such that the ratio $\frac{\langle\chi\rangle}{\Lambda} < 1$.

The flavour phenomenology of the flavon field of the FN mechanism based on $\mathscr{Z}_N \times \mathscr{Z}_M$ flavour symmetry is determined by the scale Λ. The flavon field can impact flavour observables by contributing into various flavour violating processes such as neutral meson mixing and *CP*-violation, meson decays, and charged lepton flavour violating effects. These effects could be detectable if the scale Λ is relatively low, closer to the weak scale. In such a scenario, a critical question would be how low the scale Λ can be, while still satisfying constraints from flavour physics data.

To address this, in this chapter[1], we discuss the constraints on the parameter space of the $\mathscr{Z}_N \times \mathscr{Z}_M$ flavour symmetry by taking into account both the current as well as projected sensitivities from future measurements of various quark and lepton flavour-violating observables. We created `Mathematica` packages to investigate the flavour bounds on all the $\mathscr{Z}_N \times \mathscr{Z}_M$ models discussed in this chapter.

The chapter is organized as follows: In Section 3.1, we examine the constraints on the parameter space of the flavon for various realizations of the $\mathscr{Z}_N \times \mathscr{Z}_M$ flavour symmetry, as imposed by quark flavour-violating observables. These include processes such as neutral meson mixing and meson decays into lepton pairs. Section 3.2 focuses on the constraints arising from observables related to lepton flavour-violating processes. Finally, in Section 3.3, we present a summary of the flavour bounds for each realization of the $\mathscr{Z}_N \times \mathscr{Z}_M$ flavour symmetry.

3.1 Quark flavour physics constraints on the flavon of the $\mathscr{Z}_N \times \mathscr{Z}_M$ flavour symmetries

In this section, we thoroughly investigate the bounds on the parameter space of the $\mathscr{Z}_N \times \mathscr{Z}_M$ flavour symmetries using the quark-flavour physics data. We shall present the bounds on the flavon VEV f and mass of the pseudoscalar field m_a in both soft symmetry-breaking as well as symmetry-preserving scenarios.

We note that the bounds on the parameter space of flavons of different $\mathscr{Z}_N \times \mathscr{Z}_M$ flavour symmetries from quark and leptonic flavour observables, in general, can be understood in terms of a generic behavior of the corresponding Wilson coefficients. The Wilson coefficients, in general, behave as $y_{ij}\varepsilon^{n_{ij}} y_{ji}\varepsilon^{n_{ji}}/f^2$, where y_{ij} are the dimensionless couplings of flavons with a fermionic pair. Thus, a small contribution

[1]This chapter is based on the paper Eur.Phys.J.C 83 (2023) 4, 305, and Phys.Rev.D 110 (2024) 11, 115015 in part.

of the Wilson coefficient from the flavon to the corresponding observable, such as kaon mixing, can be accommodated by either increasing the value of the VEV f, or changing the values of the coupling y_{ij} and the order parameter ε while keeping a low value of the flavon VEV f. We shall analyze the constraints arising from quark and lepton flavour physics by employing the above observation.

3.1.1 Neutral meson mixing

The neutral meson-antimeson mixing receives a contribution from the FCNC interactions occurring at the tree-level due to the non-diagonal couplings of the flavon to fermions. This contribution can be incorporated by writing the following $\Delta F = 2$ effective Hamiltonian,

$$\begin{aligned}\mathscr{H}_{\rm NP}^{\Delta F=2} = {} & C_1^{ij}\,(\bar{q}_L^i\,\gamma_\mu\,q_L^j)^2 + \widetilde{C}_1^{ij}\,(\bar{q}_R^i\,\gamma_\mu\,q_R^j)^2 + C_2^{ij}\,(\bar{q}_R^i\,q_L^j)^2 + \widetilde{C}_2^{ij}\,(\bar{q}_L^i\,q_R^j)^2 \\ & + C_4^{ij}\,(\bar{q}_R^i\,q_L^j)\,(\bar{q}_L^i\,q_R^j) + C_5^{ij}\,(\bar{q}_L^i\,\gamma_\mu\,q_L^j)\,(\bar{q}_R^i\,\gamma^\mu\,q_R^j) + \text{H.c.}, \end{aligned} \tag{3.1}$$

where $q_{R,L} = \frac{1\pm\gamma_5}{2} q$, and we do not show the colour indices for simplicity.

The Wilson coefficients corresponding to the tree-level contribution to neutral meson mixing due to the flavon exchange read as [147, 148],

$$\begin{aligned} C_2^{ij} &= -(y_{ji}^*)^2 \left(\frac{1}{m_s^2} - \frac{1}{m_a^2}\right) \\ \tilde{C}_2^{ij} &= -y_{ij}^2 \left(\frac{1}{m_s^2} - \frac{1}{m_a^2}\right) \\ C_4^{ij} &= -\frac{y_{ij}y_{ji}}{2} \left(\frac{1}{m_s^2} + \frac{1}{m_a^2}\right), \end{aligned} \tag{3.2}$$

where m_s and m_a represent the masses of scalar and pseudoscalar degrees of the flavon field.

G_F	1.166×10^{-5} GeV [152]	v	246.22 GeV [152]
$\alpha_s[M_Z]$	0.1184 [153]	m_u	$(2.16^{+0.49}_{-0.26}) \times 10^{-3}$ GeV [152]
M_W	80.387 ± 0.016 GeV [152]	m_d	$(4.67^{+0.48}_{-0.17}) \times 10^{-3}$ GeV [152]
f_K	159.8 MeV [149]	m_c	1.27 ± 0.02 GeV [152]
m_K	497.611 ± 0.013 MeV [152]	m_s	$93.4^{+8.6}_{-3.4}$ GeV [152]
$\hat{B_K}$	0.7625 [153]	m_t	172.69 ± 0.30 GeV [152]
B_1^K	0.60(6) [149]	m_b	$4.18^{+0.03}_{-0.02}$ GeV [152]
B_2^K	0.66(4) [149]	$m_c(m_c)$	1.275 GeV
B_3^K	1.05(12) [149]	$m_b(m_b)$	4.18 GeV
B_4^K	1.03(6) [149]	$m_t(m_t)$	162.883 GeV
B_5^K	0.73(10) [149]	α	1/137.035 [152]
η_1	1.87 ± 0.76 [154]	e	0.302862 GeV
η_2	0.574 [155]	m_e	0.51099 MeV [152]
η_3	0.496 ± 0.047 [156]	m_μ	105.65837 MeV [152]
f_{B_s}	230.3 MeV [153]	m_τ	1776.86 ± 0.12 MeV [152]
m_{B_s}	5366.88 MeV [152]	τ_μ	2.196811×10^{-6} sec [152]
$\hat{B_{B_s}}$	1.232[153]	τ_τ	$(290.3 \pm 0.5) \times 10^{-15}$ sec [152]
$B_1^{B_s}$	$0.86(2)(^{+5}_{-4})$ [150]	m_p	938.272 MeV [152]
$B_2^{B_s}$	0.83(2)(4) [150]	m_n	939.565 MeV [152]
$B_3^{B_s}$	1.03(4)(9) [150]	m_D	1864.83 MeV [152]
$B_4^{B_s}$	$1.17(2)(^{+5}_{-7})$ [150]	f_D	212 MeV[153]
$B_5^{B_s}$	$1.94(3)(^{+23}_{-7})$ [150]	B_1^D	0.861 [151]
η_{2B}	0.551 [155]	B_2^D	0.82 [151]
f_{B_d}	190.0 MeV [153]	B_3^D	1.07 [151]
m_{B_d}	5279.65 MeV [152]	B_4^D	1.08 [151]
$\hat{B_{B_d}}$	1.222[153]	B_5^D	1.455 [151]
$B_1^{B_d}$	$0.87(4)(^{+5}_{-4})$ [150]	τ_{B_d}	$(1.520 \pm 0.004) \times 10^{-12}$ sec [157]
$B_2^{B_d}$	0.82(3)(4) [150]	τ_{B_s}	$(1.505 \pm 0.005) \times 10^{-12}$ sec [157]
$B_3^{B_d}$	1.02(6)(9) [150]	τ_{K_L}	$(5.116 \pm 0.021) \times 10^{-8}$ sec [152]
$B_4^{B_d}$	$1.16(3)(^{+5}_{-7})$ [150]	τ_D	$(410.1 \pm 1.5) \times 10^{-15}$ sec [152]
$B_5^{B_d}$	$1.91(4)(^{+22}_{-7})$ [150]		

Table 3.1 The numerical values of the used input parameters in this work.

We evolve down the Wilson coefficients C_i from a scale Λ to the hadronic scales, used in the lattice computations of the corresponding matrix elements [149–151], 4.6 GeV for bottom mesons, 2.8 GeV for charmed mesons, and 2 GeV for kaons. The renormalization group running of the matrix elements is performed using the

procedure discussed in reference [151], and matrix elements are adopted from reference [149, 150]. Thus, the $B_q - \bar{B}_q$ mixing amplitudes beyond the SM can be written as [151],

$$\langle \bar{B}_q | \mathscr{H}_{\rm eff}^{\Delta B=2} | B_q \rangle_i = \sum_{j=1}^{5} \sum_{r=1}^{5} \left(b_j^{(r,i)} + \eta \, c_j^{(r,i)} \right) \eta^{a_j} \, C_i(\Lambda) \, \langle \bar{B}_q | Q_r^{bq} | B_q \rangle \,, \tag{3.3}$$

where $q = d, s$, $\eta = \alpha_s(\Lambda)/\alpha_s(m_t)$, a_j, $b_j^{(r,i)}$, $c_j^{(r,i)}$ denote the so-called magic numbers taken from reference [158], and α_s is the strong coupling constant. A similar expression can be written for the $D^0 - \bar{D}^0$ for which the magic numbers are present in reference [151]. The corresponding expression for the $K^0 - \bar{K}^0$ mixing reads as [151],

$$\langle \bar{K}^0 | \mathscr{H}_{\rm eff}^{\Delta S=2} | K^0 \rangle_i = \sum_{j=1}^{5} \sum_{r=1}^{5} \left(b_j^{(r,i)} + \eta \, c_j^{(r,i)} \right) \eta^{a_j} \, C_i(\Lambda) \, R_r \, \langle \bar{K}^0 | Q_1^{sd} | K^0 \rangle, \tag{3.4}$$

where R_r denotes the ratio of the matrix elements of NP operators over that of the SM [159]. The numerical values of R_r can be found in reference [151]. For the $K^0 - \bar{K}^0$ mixing, the magic numbers are used from reference [149].

For constraining the flavon mass and the VEV, we use the experimental measurements of the mixing observables of the $K^0 - \bar{K}^0$ mixing, which is given as [151],

$$C_{\varepsilon_K} = \frac{{\rm Im}\langle K^0 | \mathscr{H}_{\rm eff}^{\Delta F=2} | \bar{K}^0 \rangle}{{\rm Im}\langle K^0 | \mathscr{H}_{\rm SM}^{\Delta F=2} | \bar{K}^0 \rangle} = 1.12^{+0.27}_{-0.25}, C_{\Delta m_K} = \frac{{\rm Re}\langle K^0 | \mathscr{H}_{\rm eff}^{\Delta F=2} | \bar{K}^0 \rangle}{{\rm Re}\langle K^0 | \mathscr{H}_{\rm SM}^{\Delta F=2} | \bar{K}^0 \rangle} = 0.93^{+1.14}_{-0.42}, \tag{3.5}$$

where $\mathscr{H}_{\rm eff}^{\Delta F=2}$ represents the SM and flavon contributions, and $\mathscr{H}_{\rm SM}^{\Delta F=2}$ denotes only the SM contribution.

The $B_q - \bar{B}_q$ mixing observables are,

$$C_{B_q} e^{2i\phi_{B_q}} = \frac{\langle B_q^0 | \mathscr{H}^{\Delta F=2} | \bar{B}_q^0 \rangle}{\langle B_q^0 | \mathscr{H}_{\rm SM}^{\Delta F=2} | \bar{B}_q^0 \rangle},$$

where $q = s, d$ for the B_s and B_d mixing, respectively.

We use the following measurements at 95 % CL limits in this work [151],

$$\begin{aligned} C_{B_s} &= 1.110 \pm 0.090\ [0.942, 1.288], \quad & \phi_{B_s}^o &= 0.42 \pm 0.89\ [-1.35, 2.21] \\ C_{B_d} &= 1.05 \pm 0.11\ [0.83, 1.29], & \phi_{B_d}^o &= -2.0 \pm 1.8\ [-6.0, 1.5]. \end{aligned} \tag{3.6}$$

We write the new physics contributions to neutral meson mixing in the following form,

$$M_{12}^{d,s,K} = (M_{12}^{d,s,K})_{\rm SM} \left(1 + h_{d,s,K} e^{2i\sigma_{d,s,K}}\right). \tag{3.7}$$

The following future sensitivity phases are adopted in this work [160]:

1. Phase I which corresponds to $50 fb^{-1}$ LHCb and $50 ab^{-1}$ Belle II (late 2020s);
2. Phase II which corresponds to $300 fb^{-1}$ LHCb and $250 ab^{-1}$ Belle II (late 2030s).

Observables	Phase I	Phase II	Ref.
h_d	$0 - 0.04$	$0 - 0.028$	[160]
h_s	$0 - 0.036$	$0 - 0.025$	[160]
h_K	$0 - 0.3$	–	[**?**]

Table 3.2 The future projected sensitivities of the neutral meson mixing.

In table 3.2, we show the expected sensitivities to the observables $C_{\Delta m_K}$ and C_{B_q} in the future phase I and II of the LHCb and the Belle II.

Now, we discuss the bounds on the parameter space of the flavon of the $\mathscr{Z}_N \times \mathscr{Z}_M$ flavour symmetries arising from the neutral meson mixing. We discuss these bounds

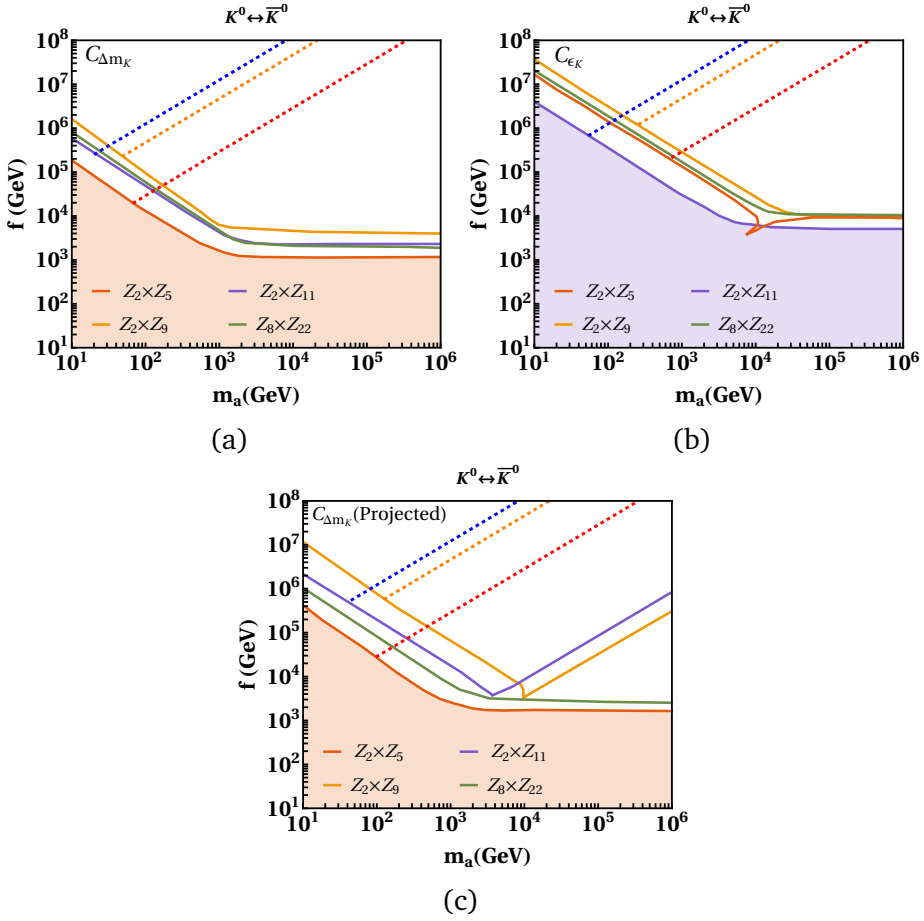

Fig. 3.1 Bounds on the parameter space of the flavon of different $\mathscr{Z}_N \times \mathscr{Z}_M$ flavour symmetries in $f - m_a$ plane from the neutral-kaon oscillations. On the top left, we show the constraints arising from the observable $C_{\Delta m_K}$, and on the top right, the bounds from the observable C_{ε_K} are shown for the value $\lambda_\chi = 2$. The figure 3.1c depicts the allowed parameter space for projected sensitivities of $C_{\Delta m_K}$ in the LHCb Phase-I. The blank region above the continuous curves in figures shows the allowed $f - m_a$ parameter space in the soft symmetry-breaking framework, while the dashed curves are allowed for the symmetry-preserving scenario as defined by equation 2.49. The colored region below the continuous curves indicates the $f - m_a$ parameter space excluded by all four $\mathscr{Z}_N \times \mathscr{Z}_M$ models in the soft symmetry-breaking scenario.

simultaneously for the soft symmetry-breaking as well as the symmetry-conserving scenarios. In figure 3.1, we show the bounds on the parameter space of the flavon corresponding to different $\mathscr{Z}_N \times \mathscr{Z}_M$ flavour symmetries from neutral kaon mixing observable $C_{\Delta m_K}$ on the left, and that from the observable C_{ε_K} on the right

for the quartic coupling $\lambda_\chi = 2$. The region above the continuous curves show the allowed parameter space in the soft symmetry-breaking scenario for different $\mathscr{Z}_N \times \mathscr{Z}_M$ flavour symmetries. On the other side, the dashed curves represent symmetry-conserving scenario defined by equation 2.49. In the case of the soft symmetry-breaking scenario, the shaded region of the parameter space below the continuous curves is excluded by the corresponding observables. The symmetry-conserving scenario turns out to be extremely predictive in the sense that the allowed flavon parameter space is only along the dashed straight lines, and the rest of the region is excluded by the corresponding observables.

We observe that the bounds from the observable $C_{\Delta m_K}$ are most stringent for the flavour symmetry $\mathscr{Z}_2 \times \mathscr{Z}_9$, shown by the region above yellow-coloured continuous curve in figure 3.1a. This is followed by the $\mathscr{Z}_2 \times \mathscr{Z}_{11}$ and $\mathscr{Z}_8 \times \mathscr{Z}_{22}$ flavour symmetries for which the allowed parameter space is almost similar, shown in figure 3.1a by the region above the violet and green coloured continuous curves, respectively. The bounds become more stringent when the observable C_{ε_K} is used as shown in figure 3.1b. The most stringent bounds continue to be for the $\mathscr{Z}_2 \times \mathscr{Z}_9$ flavour symmetry even from the observable C_{ε_K}. The bounds from the observable C_{ε_K} on the flavour symmetries $\mathscr{Z}_2 \times \mathscr{Z}_5$ and $\mathscr{Z}_8 \times \mathscr{Z}_{22}$ are very close and are more stringent than that of the $\mathscr{Z}_2 \times \mathscr{Z}_{11}$ flavour symmetry, shown by the blue continuous curve. In figure 3.1c, we show the bounds on the parameter space of the flavon of different $\mathscr{Z}_N \times \mathscr{Z}_M$ flavour symmetries for the projected future sensitivities of the neutral meson mixing given in table 3.2 for the soft symmetry-breaking and symmetry-conserving scenario again by the solid continuous curves.

In figures 3.1a and 3.1c, the bounds corresponding to the $\mathscr{Z}_2 \times \mathscr{Z}_5$ flavour symmetry are relatively loose from the observable $C_{\Delta m_K}$. The reason for this is a low value of the order parameter $\varepsilon = 0.1$, which dominates the behavior of the Wilson

coefficients, in general, and allows a low value of the flavon VEV f. The symmetries $\mathscr{Z}_{2,8} \times \mathscr{Z}_{9,11,22}$ are showing a similar behavior since the order parameter ε is very close for them. On the other side, in figure 3.1b the contribution from the imaginary part of the product $y_{ij}y_{ij}$ is very large for the $\mathscr{Z}_2 \times \mathscr{Z}_5$ flavour symmetry, making it closer to the predictions of $\mathscr{Z}_{2,8} \times \mathscr{Z}_{9,22}$ symmetries. The symmetry-conserving scenario is dominated by the values of the parameter ε, leading to the strongest bounds for the $\mathscr{Z}_2 \times \mathscr{Z}_{9,11}$ flavour symmetries. This is a generic observation in the sense that it will continue to show up even for leptonic flavour observables except for the D^0 mixing. Therefore, we shall discuss it only for the D^0 mixing later.

For the symmetry-conserving scenario, the most stringent bounds from the observable $C_{\Delta m_K}$ again appear for the $\mathscr{Z}_2 \times \mathscr{Z}_9$ flavour symmetry denoted by the orange dashed line in figure 3.1a. We must note that for the symmetry-conserving case, the dashed straight lines are the only allowed parameter space, and the rest of the region is excluded by the corresponding mixing observables. The bounds for the projected future sensitivities of the neutral meson mixing given in table 3.2 in the case of the symmetry-conserving scenario are shown by the dashed straight lines in figure 3.1c for different $\mathscr{Z}_N \times \mathscr{Z}_M$ flavour symmetries.

The bounds on the parameter space of the flavon of the $\mathscr{Z}_N \times \mathscr{Z}_M$ flavour symmetries arising from the neutral B_s-meson mixing are represented in figure 3.2. On the left in figure 3.2a, we show the constraints on the parameter space of the flavon derived from the observable C_{B_s}. For the soft symmetry-breaking case, the bounds are depicted by the solid continuous curves, and the region below these curves is excluded by the experimental measurement of the observable C_{B_s}. We notice that the observable C_{B_s}, unlike the neutral-kaon mixing, which was more constraining to the $\mathscr{Z}_2 \times \mathscr{Z}_9$ flavour symmetry, place stronger bounds on the $\mathscr{Z}_2 \times \mathscr{Z}_{11}$ flavour symmetry for the flavon mass approximately below 1 TeV. Above

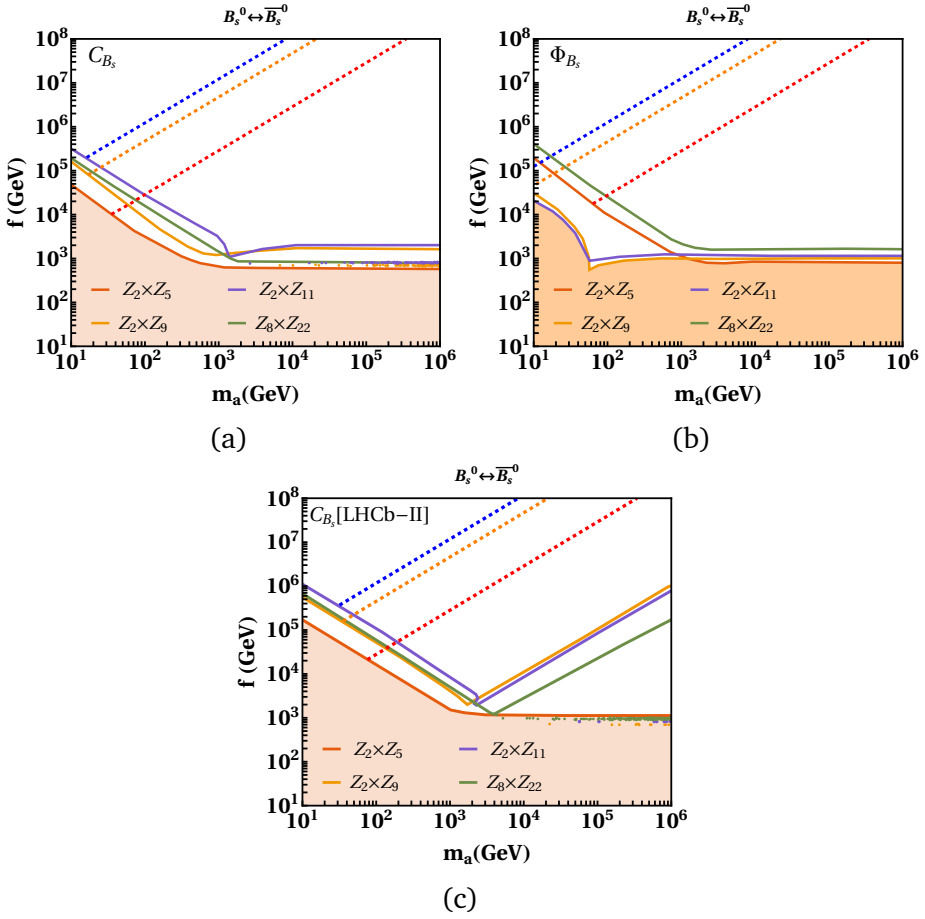

Fig. 3.2 Bounds on the parameter space of the flavon of different $\mathscr{Z}_N \times \mathscr{Z}_M$ flavour symmetries in $f - m_a$ plane from the neutral B_s-meson mixing. On the top left, we show the constraints arising from the observable C_{B_s}, and on the top right, the bounds from the observable Φ_{B_s} are shown for the value $\lambda_\chi = 2$. The figure 3.2c depicts the allowed parameter space for projected sensitivities of C_{B_s} in the LHCb Phase-II. Moreover, the region above the continuous curves represent the allowed $f - m_a$ parameter space in the soft symmetry-breaking framework, and dashed curves are for the symmetry-preserving scenario defined by equation 2.49. The colored region below the continuous curves indicates the $f - m_a$ parameter space excluded by all four $\mathscr{Z}_N \times \mathscr{Z}_M$ models in the soft symmetry-breaking scenario.

the flavon mass 1 TeV, the bounds are similar for the $\mathscr{Z}_2 \times \mathscr{Z}_{11}$ and $\mathscr{Z}_2 \times \mathscr{Z}_9$ flavour symmetries. The observable Φ_{B_s} is more suitable to constrain the parameter space corresponding to the $\mathscr{Z}_8 \times \mathscr{Z}_{22}$ flavour symmetry, as observed in figure 3.2b. The future projected sensitivity of the observable C_{B_s} in the LHCb phases-I, II further constrains the parameter space corresponding to the $\mathscr{Z}_2 \times \mathscr{Z}_{11}$ flavour symmetry for

the flavon mass approximately up to 1 TeV. The constraints for the future projected sensitivity of the observable C_{B_s} in the LHCb phase-I are almost similar to that of phase-II. Therefore, we show them only for phase-II in this work. Above the flavon mass 1 TeV, the bounds are further stronger and again similar for the $\mathscr{Z}_2 \times \mathscr{Z}_{11}$ and $\mathscr{Z}_2 \times \mathscr{Z}_9$ flavour symmetries.

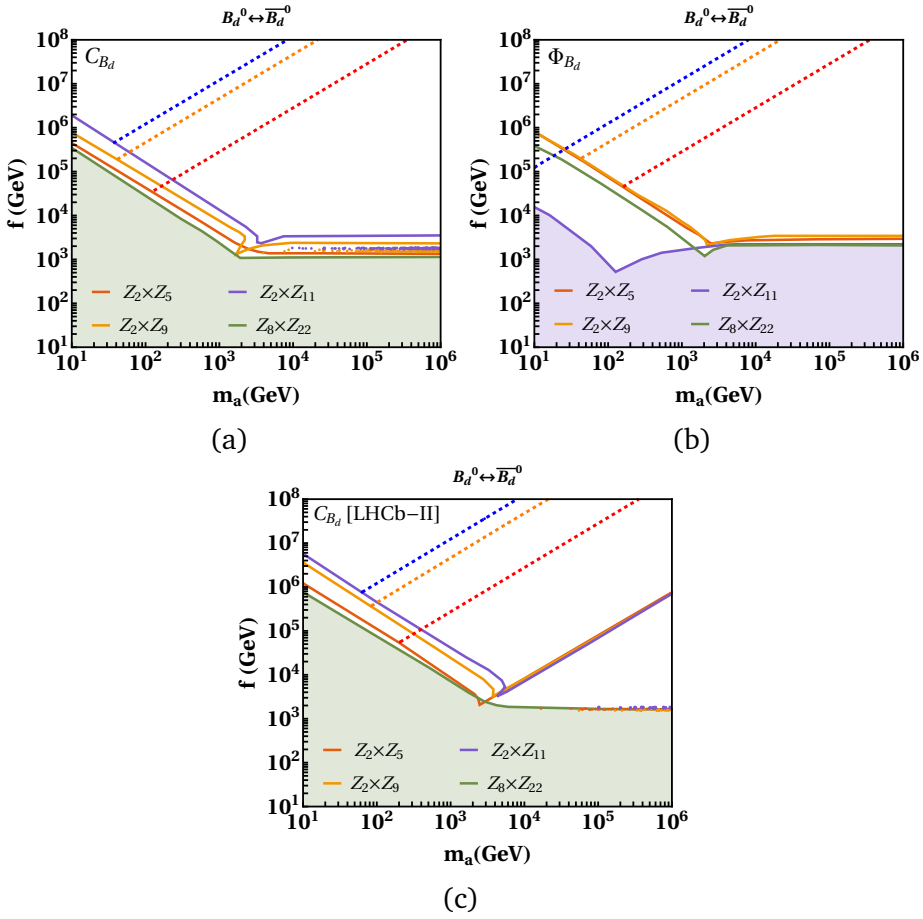

Fig. 3.3 Bounds on the parameter space of the flavon of different $\mathscr{Z}_N \times \mathscr{Z}_M$ flavour symmetries in $f - m_a$ plane from the neutral B_d-meson mixing. On the top left, we show the constraints arising from the observable C_{B_d}, and on the right, the bounds from the observable Φ_{B_d} are shown for the value $\lambda_\chi = 2$. The figure 3.3c depicts the allowed parameter space for projected sensitivities of C_{B_d} in the LHCb Phase-II. Moreover, the region above the continuous curves represent the allowed $f - m_a$ parameter space in the soft symmetry-breaking framework, and dashed curves are for the symmetry-preserving scenario defined by equation 2.49.

For the symmetry-conserving scenario, the most stringent constraints are derived for the symmetry $\mathscr{Z}_2 \times \mathscr{Z}_{11}$ from both the observables C_{B_s} and Φ_{B_s}, as shown by the dashed blue straight lines in figures 3.2a, 3.2b, and in 3.2c for the future projected sensitivity of the observable C_{B_s} in the LHCb phase-II. After the $\mathscr{Z}_2 \times \mathscr{Z}_{11}$ flavour symmetry, the parameter space corresponding to the flavon of the $\mathscr{Z}_2 \times \mathscr{Z}_9$ flavour symmetry receives the stronger bounds denoted by the orange dashed straight lines in figure 3.2.

We notice that the bounds from the observable C_{B_s} depend on the value $|y_{ij}y_{ij}|$, which is small for the $\mathscr{Z}_2 \times \mathscr{Z}_5$ flavour symmetry allowing a large parameter space for the order parameter $\varepsilon = 0.1$. The parameter ε is largest for the $\mathscr{Z}_2 \times \mathscr{Z}_{11}$ flavour symmetry resulting in the most stringent bounds. The bounds for the rest of the symmetries are closer to that of the $\mathscr{Z}_2 \times \mathscr{Z}_{11}$ flavour symmetry due to the closer value of the ε parameter. The observable Φ_{B_s} is sensitive to the $\arg(y_{ij}y_{ij})$, which is large for the $\mathscr{Z}_2 \times \mathscr{Z}_5$ flavour symmetry leading to a more constrained parameter space, which is close to that of the $\mathscr{Z}_8 \times \mathscr{Z}_{22}$ flavour symmetry. The value of the $\arg(y_{ij}y_{ij})$ is small and close for the $\mathscr{Z}_2 \times \mathscr{Z}_{9,11}$ flavour symmetries producing similar bounds.

For the B_d-meson mixing, we can make observations similar to that of the B_s-meson mixing discussed earlier. The absolute values of the product $|y_{ij}y_{ij}|$ together with the value of the parameter ε determines the bounds from the observable C_{B_d}. On the other side, the $\arg(y_{ij}y_{ij})$ together with the value of the parameter ε determines the bounds from the observable Φ_{B_d}.

Thus, the observable C_{B_d} places the most stringent bounds on the parameter space of the flavon of the $\mathscr{Z}_2 \times \mathscr{Z}_{11}$ flavour symmetry for the soft symmetry-breaking scenario, as shown in figure 3.3a. This observation is similar to that obtained from the neutral B_s-meson mixing in figure 3.2. This feature continues to be seen even in

the future projected sensitivity of the observable C_{B_d} in the LHCb phase-II, as shown in figure 3.3c. The bounds for the future projected sensitivity of the observable C_{B_d} in the LHCb phase-I are very similar to that of phase-II. Therefore, we do not show them in this work. On the other side, the observable Φ_{B_d} provides more stringent bounds on the parameter space of the flavon of the $\mathscr{Z}_2 \times \mathscr{Z}_{5,9}$ flavour symmetries for the soft symmetry-breaking scenario as shown in figure 3.3b.

In the symmetry-conserving scenario, the B_d-meson mixing places bounds on the parameter space of the flavon of $\mathscr{Z}_N \times \mathscr{Z}_M$ flavour symmetries similar to that of the B_s-meson mixing, as can be observed from figure 3.3a-3.3c, where the allowed parameter space is shown by dashed straight lines. The strongest bounds in this case turn out to be for the flavon of the $\mathscr{Z}_2 \times \mathscr{Z}_{11}$ flavour symmetry, followed by the flavon of the $\mathscr{Z}_2 \times \mathscr{Z}_9$ flavour symmetry.

Large hadronic uncertainties exist in the SM contribution of the $D^0 - \bar{D}^0$ mixing. For this reason, the flavon contribution to the $D^0 - \bar{D}^0$ mixing is chosen to lie within the 2σ experimental bound [161], that is,

$$|M_{12}^D| = |\langle D^0|\mathscr{H}^{\Delta F=2}|\bar{D}^0\rangle| < 7.5 \times 10^{-3} ps^{-1} \tag{3.8}$$

In figure 3.4, we show the bounds arising from the D-meson mixing. In this case, the absolute values of the product $|y_{ij}y_{ij}|$ dictate the behavior of bounds from the observable $|M_{12}^D|$. For instance, the absolute values of the product $|y_{ij}y_{ij}|$ is very large for the $\mathscr{Z}_2 \times \mathscr{Z}_5$ flavour symmetry, leading to more stringent bounds for the soft symmetry-breaking, as well as for the symmetry-conserving scenarios.

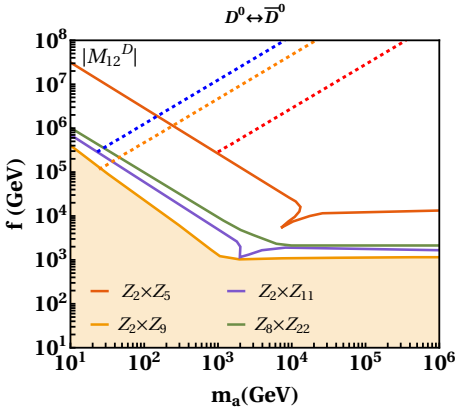

Fig. 3.4 Bounds on the parameter space of the flavon of different $\mathscr{Z}_N \times \mathscr{Z}_M$ flavour symmetries in $f - m_a$ plane from the neutral $D^0 - \bar{D}^0$ meson mixing for the soft symmetry-breaking as well as for the symmetry-conserving scenarios for $\lambda_\chi = 2$.

3.1.2 Two body leptonic decays of pseudoscalar mesons

The two-body leptonic decays of a pseudoscalar meson into charged leptons can be described by the following effective Hamiltonian,

$$\mathscr{H}_{\text{eff}} = -\frac{G_F^2 m_W^2}{\pi^2}\left(C_S^{ij}\,(\bar{q}_i P_L q_j)\bar{\ell}\ell + \tilde{C}_S^{ij}\,(\bar{q}_i P_R q_j)\bar{\ell}\ell + C_P^{ij}(\bar{q}_i P_L q_j)\bar{\ell}\gamma_5\ell + \tilde{C}_P^{ij}(\bar{q}_i P_R q_j)\bar{\ell}\gamma_5\ell\right) + \text{H.c.}. \tag{3.9}$$

The branching ratio for such a leptonic decay of meson can be written as,

$$\text{BR}(M \to \ell^+\ell^-) = \frac{G_F^4 m_W^4}{8\pi^5}\beta\, m_M f_M^2 m_\ell^2 \tau_M \left(\left|\frac{m_M^2\left(C_P^{ij} - \tilde{C}_P^{ij}\right)}{2m_\ell(m_i + m_j)} - C_A^{\text{SM}}\right|^2 + \left|\frac{m_M^2\left(C_S^{ij} - \tilde{C}_S^{ij}\right)}{2m_\ell(m_i + m_j)}\right|^2 \beta^2\right), \tag{3.10}$$

where $\beta(x) = \sqrt{1-4x^2}$ with $x = m_\ell/m_M$.

The tree-level contribution of the flavon to the corresponding Wilson coefficients reads as [147, 148],

$$
\begin{aligned}
C_S^{ij} &= \frac{\pi^2}{2G_F^2 m_W^2} \frac{2y_{\ell\ell} y_{ji}}{m_s^2} \\
\tilde{C}_S^{ij} &= \frac{\pi^2}{2G_F^2 m_W^2} \frac{2y_{\ell\ell} y_{ij}}{m_s^2} \\
C_P^{ij} &= \frac{\pi^2}{2G_F^2 m_W^2} \frac{2y_{\ell\ell} y_{ji}}{m_a^2} \\
\tilde{C}_P^{ij} &= \frac{\pi^2}{2G_F^2 m_W^2} \frac{2y_{\ell\ell} y_{ij}}{m_a^2}.
\end{aligned} \tag{3.11}
$$

In the SM, the two-body leptonic decays of a pseudoscalar meson into two charged leptons occur at one-loop, and their contribution is given by [148],

$$
C_A^{\mathrm{SM}} = -V_{tb}^* V_{ts} Y\left(\frac{m_t^2}{m_W^2}\right) - V_{cb}^* V_{cs} Y\left(\frac{m_c^2}{m_W^2}\right), \tag{3.12}
$$

where $Y(x)$ is the Inami-Lim function, given by [162],

$$
Y(x) = \eta_{\mathrm{QCD}} \frac{x}{8}\left[\frac{4-x}{1-x} + \frac{3x}{(1-x)^2}\log x\right], \tag{3.13}
$$

where $\eta_{\mathrm{QCD}} = 1.0113$ shows the NLO QCD effects [163]. For B_d meson, the SM predictions can be obtained by replacing the indices in equation 3.12.

The $B_{s,d}$ meson decays

The HFLAV group provides the branching fraction of $B_s \to \mu^+\mu^-$ to be [164],

$$
\mathrm{BR}(B_s \to \mu^+\mu^-) = (3.45 \pm 0.29) \times 10^{-9}. \tag{3.14}
$$

The branching ratio of the $B_d \to \mu^+\mu^-$ decay is [165, 166],

$$\mathrm{BR}(B_d \to \mu^+\mu^-) < 2.6 \times 10^{-10}. \tag{3.15}$$

To convert the theoretical branching ratio of the B_s meson to the experimental branching ratio, we multiply by the factor $(1-y_s)^{-1}$ [167], where $y_s = 0.088 \pm 0.014$ [168]. This is done due to the sizeable width difference of the B_s meson, and this correction can be ignored in the case of the B_d meson.

Observables	Current	LHCb-I	LHCb-II	CMS	ATLAS
$\mathrm{BR}(B_s \to \mu^+\mu^-)(\times 10^9)$	± 0.38	± 0.30	± 0.16	–	± 0.50
$\mathscr{R}_{\mu\mu}$	$\sim 70\%$	$\sim 34\%$	$\sim 10\%$	$\sim 21\%$	–
$\tau_{\mu\mu}$	$\sim 12\%$	± 0.16 ps	± 0.04 ps	–	–

Table 3.3 The values of the rare B decays observables for the current and expected experimental precision. The LHCb-I corresponds to $23 fb^{-1}$, LHCb-II corresponds to $300 fb^{-1}$, and the CMS and the ATLAS correspond to $3 ab^{-1}$[169, 170].

We note that the LHCb collaboration has also measured the ratio of the $\mathrm{BR}(B_d \to \mu^+\mu^-)$ and $\mathrm{BR}(B_s \to \mu^+\mu^-)$ branching fractions, $\mathscr{R}_{\mu\mu}$[165, 166]. This observable can also be used to constrain the parameter space of flavon of different $\mathscr{Z}_N \times \mathscr{Z}_M$ flavour symmetries, and we shall show later that it provides the striking bounds of the parameter space of flavon of different $\mathscr{Z}_N \times \mathscr{Z}_M$ flavour symmetries. It should be noted that the ratio $\mathscr{R}_{\mu\mu}$ turns out to be an excellent observable to probe the minimal flavour violation[170]. Moreover, the effective lifetime, $\tau_{\mu\mu}$, of the $B_s \to \mu^+\mu^-$ decay is also measured by the CMS [169]. The effective lifetime, $\tau_{\mu\mu}$, is capable of distinguishing between the contributions due to any possible new scalar and pseudoscalar mediators [170].

The ratio of branching fractions, $\mathscr{R}_{\mu\mu}$ is [165, 166],

$$\mathscr{R}_{\mu\mu} = \frac{\mathrm{BR}(B_d \to \mu^+\mu^-)}{\mathrm{BR}(B_s \to \mu^+\mu^-)} = 0.039^{+0.030+0.006}_{-0.024-0.004}. \tag{3.16}$$

The CMS has measured the effective lifetime $\tau_{\mu\mu}$ and the branching fraction of $B_s \to \mu^+\mu^-$, which are [169],

$$\tau_{\mu\mu} = 1.83^{+0.23+0.04}_{-0.20-0.04}\ \text{ps}, \tag{3.17}$$

$$\text{BR}(B_s \to \mu^+\mu^-) = 3.83^{+0.38+0.19+0.14}_{-0.36-0.16-0.13} \times 10^{-9}. \tag{3.18}$$

The HFLAV measurement average of the effective lifetime $\tau_{\mu\mu}$ is [164],

$$\tau_{\mu\mu} = 2.00^{+0.27}_{-0.26}\ \text{ps}, \tag{3.19}$$

with $\text{BR}(B_s \to \mu^+\mu^-)$ given in equation 3.14.

We summarize the current and future sensitivities of these observables in table 3.3. The effective lifetime can be expressed as [171],

$$\tau_{\mu\mu} = \frac{\tau_{B_s}}{1-y_s^2}\left[\frac{1+2\mathscr{A}^f_{\Delta\Gamma}y_s+y_s^2}{1+\mathscr{A}^f_{\Delta\Gamma}y_s}\right]. \tag{3.20}$$

The experimentally measurable branching ratio can be related to the theoretical branching ratio as [171],

$$\text{BR}(B_s \to \mu^+\mu^-)^{\text{experiment}} = \text{BR}(B_s \to \mu^+\mu^-)^{\text{theory}}\left[\frac{1-y_s^2}{1+\mathscr{A}^f_{\Delta\Gamma}y_s}\right], \tag{3.21}$$

where the final state dependent observable is defined as [168],

$$\mathscr{A}^f_{\Delta\Gamma} = \frac{1}{y_s}\left[\frac{(1-y_s^2)\tau_{\mu\mu}-(1+y_s^2)\tau_{B_s}}{2\tau_{B_s}-(1-y_s^2)\tau_{\mu\mu}}\right]. \tag{3.22}$$

In the SM, its predicted value is $\mathscr{A}^f_{\Delta\Gamma} = 1$ [168]. Substituting this into equations 3.20 and 3.21 leads to the following expression for the effective lifetime,

$$\tau_{\mu\mu} = \tau_{B_s} \frac{\mathrm{BR}(B_s \to \mu^+\mu^-)^{\text{experiment}}}{\mathrm{BR}(B_s \to \mu^+\mu^-)^{\text{theory}}}. \tag{3.23}$$

The K_L meson decays

The short-distance (SD) part of $K_L \to \mu^+\mu^-$ decay can be estimated in a reliable manner [147]. Its SM prediction is given in reference [147], and reads as,

$$C_A^{\mathrm{SM}} = -V_{ts}^* V_{td}\, Y\left(\frac{m_t^2}{m_W^2}\right) - V_{cs}^* V_{cd} Y_{\mathrm{NNL}}, \tag{3.24}$$

where at NNLO $Y_{\mathrm{NNL}} = \lambda^4 P_c(Y)$, $\lambda = |V_{us}|$ and $P_c(Y) = 0.113 \pm 0.017$[172]. The short-distance contribution is extracted from the experimental measurement, and its upper limit is [148],

$$\mathrm{BR}(K_L \to \mu^+\mu^-)_{\mathrm{SD}} < 2.5 \times 10^{-9}. \tag{3.25}$$

The D meson decays

The SM contribution of the $D \to \mu^+\mu^-$ decay is marred by the large non-perturbative effects. Therefore, we assume that the flavon contribution to this decay rate lies within the experimental upper bound on the branching ratio, given at 90% C.L.[173],

$$\mathrm{BR}(D \to \mu^+\mu^-) < 6.2 \times 10^{-9}. \tag{3.26}$$

We note that the bounds from the two-body leptonic decays of a pseudoscalar meson depend on the product $|y_{ij}^q y_{ij}^\ell|$. This quantity is very small for the $\mathscr{Z}_2 \times \mathscr{Z}_5$

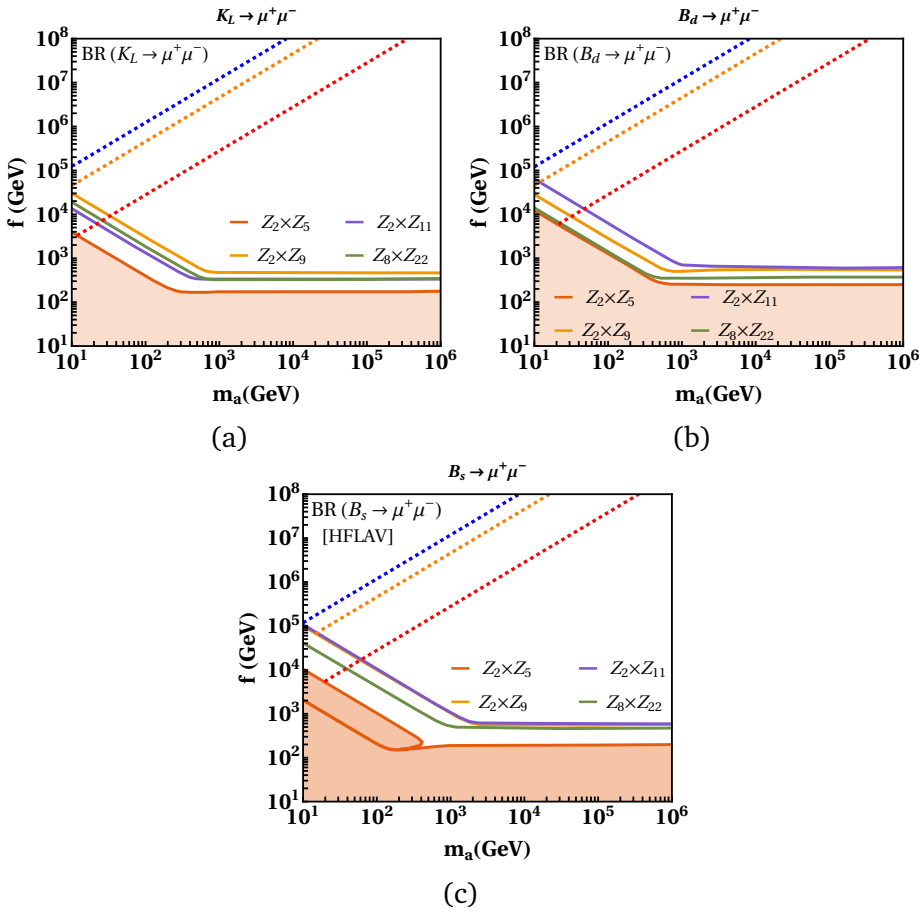

Fig. 3.5 The coloured region represents the excluded parameter space for the flavon of all four $\mathscr{Z}_N \times \mathscr{Z}_M$ flavour symmetries by the limits on branching ratios $\mathrm{BR}(K_L \to \mu^+\mu^-)_{\mathrm{SD}}$, $\mathrm{BR}(B_d \to \mu^+\mu^-)$ and the $\mathrm{BR}(B_s \to \mu^+\mu^-)$ for the soft symmetry-breaking scenario. The dashed line represents the allowed parameter space by the same observables for symmetry-conserving scenario, with $\lambda_\chi = 2$ for both the scenarios.

flavour symmetry, and closer for the rest of the flavour symmetries for the two-body leptonic decays of a pseudoscalar meson.

In figure 3.5, we show the bounds on the parameter space of flavon of different $\mathscr{Z}_N \times \mathscr{Z}_M$ flavour symmetries arising from the branching ratio of the $K_L \to \mu^+\mu^-$ decay. In the case of the soft symmetry-breaking scenario, the branching ratio of the $K_L \to \mu^+\mu^-$ decay imposes stronger bounds on the $\mathscr{Z}_2 \times \mathscr{Z}_9$ flavour symmetry. After this, the constraints are stronger for the $\mathscr{Z}_2 \times \mathscr{Z}_{11}$ flavour symmetry. The decay $B_d \to$

$\mu^+\mu^-$ constrains more parameter space of flavon of the $\mathscr{Z}_2 \times \mathscr{Z}_{11}$ flavour symmetry, followed by the $\mathscr{Z}_2 \times \mathscr{Z}_9$ flavour symmetry. On the other hand, the branching ratio of the decay $B_s \to \mu^+\mu^-$ bounds both the $\mathscr{Z}_2 \times \mathscr{Z}_9$ and $\mathscr{Z}_2 \times \mathscr{Z}_{11}$ flavour symmetries together with similar strength, while the bounds are comparatively weak in the case of $\mathscr{Z}_8 \times \mathscr{Z}_{22}$ flavour symmetry. In the symmetry-preserving scenario, all three decays place the stronger bounds on the $\mathscr{Z}_2 \times \mathscr{Z}_{11}$ flavour symmetry. This is followed by the $\mathscr{Z}_2 \times \mathscr{Z}_9$ flavour symmetry, and $\mathscr{Z}_2 \times \mathscr{Z}_5$ flavour symmetry. We do not show the bounds from $BR(D \to \mu^+\mu^-)$ as it imposes extremely weak constraint on the parameter space of all four $\mathscr{Z}_N \times \mathscr{Z}_M$ flavour symmetries.

The observable $\tau_{\mu\mu}$ places the strongest bounds on the parameter space of flavon of the $\mathscr{Z}_2 \times \mathscr{Z}_5$ flavour symmetry in the soft symmetry-breaking scenario, as observed in figure 3.6. This is expected since the lifetime is inverse of the decay-width, and the branching ratio of the decay $B_s \to \mu^+\mu^-$ places the most relaxed constraints on the flavon of the $\mathscr{Z}_2 \times \mathscr{Z}_5$ flavour symmetry. This is followed by the flavon of the $\mathscr{Z}_2 \times \mathscr{Z}_{11}$ flavour symmetry. For the symmetry-conserving scenario, the most stringent constraints arise for the flavon of the $\mathscr{Z}_2 \times \mathscr{Z}_{11}$ flavour symmetry, followed by the flavon of the $\mathscr{Z}_2 \times \mathscr{Z}_9$ flavour symmetry. There is no substantial improvement over these bounds in the future projected sensitivities of the LHCb. Therefore, we do not show them in this work.

The ratio $\mathscr{R}_{\mu\mu}$ is one of the most important observables to test the $\mathscr{Z}_N \times \mathscr{Z}_M$ flavour symmetries. Its future projected sensitivity will play a decisive role in constraining the parameter space of flavon of $\mathscr{Z}_N \times \mathscr{Z}_M$ flavour symmetries. The predictions from this observable are shown in figure 3.7. The bounds from the ratio $\mathscr{R}_{\mu\mu}$ are minimally sensitive to the product $y_{ij}\varepsilon^{n_{ij}} y_{ji}\varepsilon^{n_{ji}}$ since it appears in the numerator as well as denominator of the ratio $\mathscr{R}_{\mu\mu}$. Therefore, all the $\mathscr{Z}_N \times \mathscr{Z}_M$

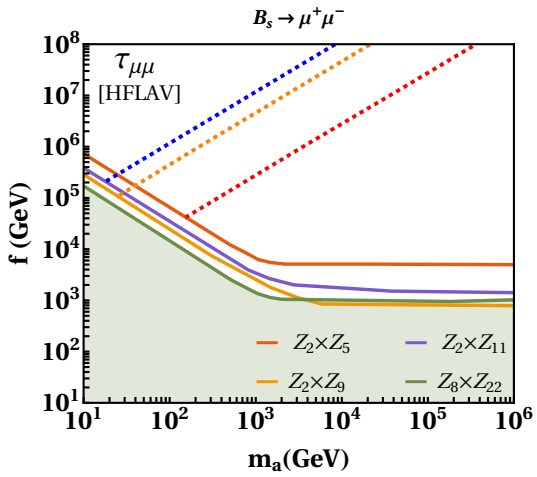

Fig. 3.6 The allowed parameter space by the observable $\tau_{\mu\mu}$ for the flavon of different $\mathscr{Z}_N \times \mathscr{Z}_M$ flavour symmetries for the recent measurement.

flavour symmetries exhibit a close behavior providing relatively relaxed bounds from the current measurements.

In the case of soft symmetry-breaking scenario, the strongest bounds turn out to be for the $\mathscr{Z}_2 \times \mathscr{Z}_9$ and $\mathscr{Z}_2 \times \mathscr{Z}_{11}$ flavour symmetries for the current measurement of the observable $\mathscr{R}_{\mu\mu}$, as observed in figure 3.7a. This feature continues to grow stronger further in the future high luminosity phase-I of the LHCb, as can be seen in figure 3.7b. In the symmetry-conserving scenario, the parameter space of the flavon of the $\mathscr{Z}_2 \times \mathscr{Z}_{11}$ is more constrained than any other flavour symmetry for the current measurement as well as for the high luminosity phase-I of the LHCb, as can be seen in figure 3.7a and 3.7b. This is followed by the $\mathscr{Z}_2 \times \mathscr{Z}_9$ flavour symmetry.

We obtain very stringent bounds on the parameter space of the flavon of different $\mathscr{Z}_N \times \mathscr{Z}_M$ flavour symmetries from the future high luminosity phase-II of the LHCb, as can be seen in figure 3.7c. We emphasize to note that the colored stripes in this figure are allowed parameter space for the soft symmetry-breaking scenario, and the blank region is the excluded parameter space. We observe from 3.7c that the allowed parameter space is very narrow and different for $\mathscr{Z}_N \times \mathscr{Z}_M$ flavour symmetries for $m_a < 1$ TeV. The stripe corresponding to the $\mathscr{Z}_2 \times \mathscr{Z}_9$ flavour

symmetry resides inside the stripe corresponding to the $\mathscr{Z}_2 \times \mathscr{Z}_5$ flavour symmetry in this case. Above $m_a > 1$ TeV, the stripes corresponding to the $\mathscr{Z}_2 \times \mathscr{Z}_9$ and $\mathscr{Z}_2 \times \mathscr{Z}_{11}$ flavour symmetries overlap around 10^4 TeV.

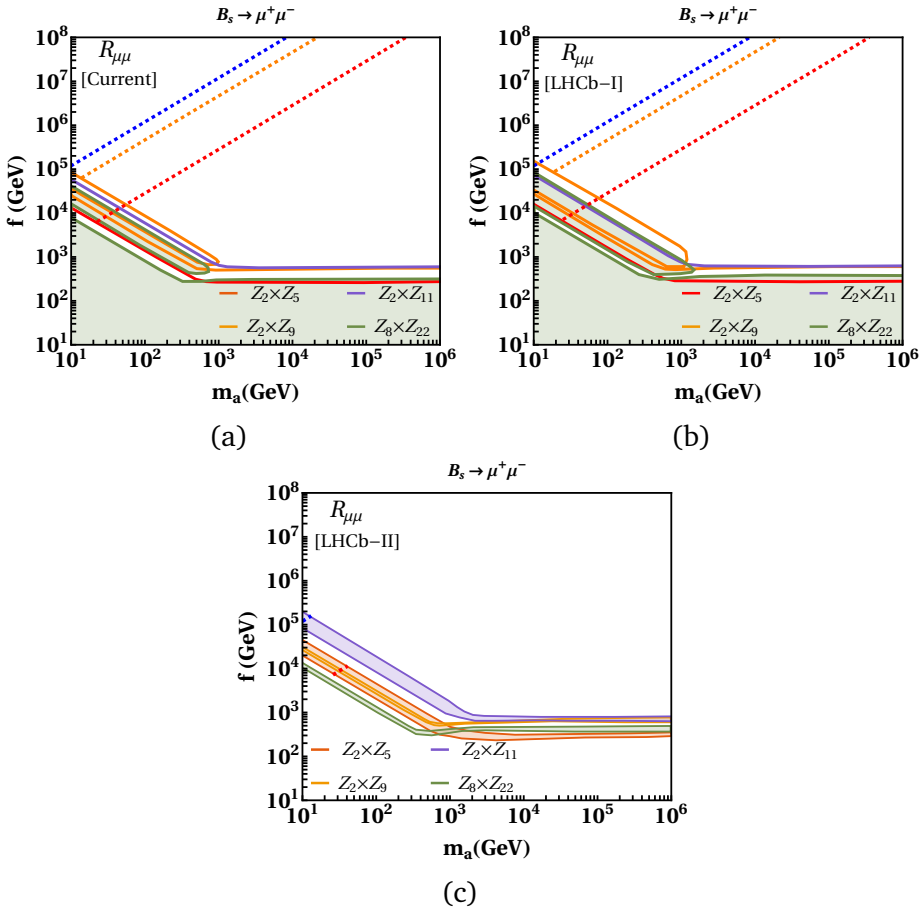

(a) (b)

(c)

Fig. 3.7 The blank region above the continuous curves in figure 3.7a and 3.7b shows the allowed $f - m_a$ parameter space of the flavon of different $\mathscr{Z}_N \times \mathscr{Z}_M$ models by current measurement as well as the future projected sensitivities in the LHCb Phase-I for the observable $\mathscr{R}_{\mu\mu}$, with $\lambda_\chi = 2$, in the soft symmetry-breaking scenario. The coloured region in figure 3.7c depicts the same allowed parameter space for projected sensitivities of $\mathscr{R}_{\mu\mu}$ in the LHCb Phase-II, while the dashed lines represent the allowed parameter space in the symmetry-conserving scenario.

The remarkable predictions are obtained in the case of the symmetry-conserving scenario. As evident from figure 3.7c, there is a very small allowed parameter space for symmetries $\mathscr{Z}_2 \times \mathscr{Z}_5$ and $\mathscr{Z}_2 \times \mathscr{Z}_{11}$, shown by the dashed-red and dashed-blue lines within the stripes, respectively. There is no allowed parameter space for other

symmetries for the symmetry-conserving scenario. Thus, the future high luminosity phase-II of the LHCb will be crucial in ruling out the symmetry-conserving scenario discussed in this work.

3.2 Leptonic flavour physics of the flavon of the $\mathscr{Z}_N \times \mathscr{Z}_M$ flavour symmetries

The current and future experiments on the charged lepton flavour violation (CLFV) processes have a great potential to place stringent bounds on the parameter space of the flavon of the $\mathscr{Z}_N \times \mathscr{Z}_M$ flavour symmetries, and even may provide an improvement over the constraints arising from the quark flavour physics. The sensitivities of the CLFV processes for the current as well as future projected experiments are shown in table 3.4. The Feynman diagrams shown in this thesis are created using `JaxoDraw`.

The bounds from the leptonic flavour physics are sensitive to the $|y^{\ell}_{ij}\varepsilon^{n_{ij}}y^{\ell}_{ji}\varepsilon^{n_{ji}}|$, which is minimum for the $\mathscr{Z}_2 \times \mathscr{Z}_5$ flavour symmetry, providing the most relaxed constraints on the flavon corresponding to this symmetry. For other flavour symmetries, the value of the $|y^{\ell}_{ij}\varepsilon^{n_{ij}}y^{\ell}_{ji}\varepsilon^{n_{ji}}|$ is close, resulting in bounds, that are close in magnitude. This is a generic observation about the leptonic flavour physics.

3.2.1 Radiative leptonic decays

We write the following effective Lagrangian for the radiative leptonic decays,

$$\mathscr{L}_{\text{eff}} = m_{\ell'} C_T^L \, \bar{\ell}\sigma^{\rho\lambda} P_L \ell' F_{\rho\lambda} + m_{\ell'} C_T^R \, \bar{\ell}\sigma^{\rho\lambda} P_R \ell' F_{\rho\lambda}. \tag{3.27}$$

Observables	Current sensitivity	Ref.	Future projection	Ref.
BR($\mu \to e\gamma$)	$< 4.2 \times 10^{-13}$	MEG [174]	6×10^{-14}	MEGII [175]
BR($\tau \to e\gamma$)	$< 3.3 \times 10^{-8}$	Babar [176]	$\sim 10^{-9}$	Belle II [177]
BR($\tau \to \mu\gamma$)	$< 4.4 \times 10^{-8}$	Babar [176]	$\sim 10^{-9}$	Belle II [177]
BR $(\mu \to e)^{\mathrm{Au}}$	$< 7 \times 10^{-13}$	SINDRUM II [178]	–	–
BR $(\mu \to e)^{\mathrm{Al}}$	–	–	3×10^{-15}	COMET Phase-I [179, 180]
BR $(\mu \to e)^{\mathrm{Al}}$	–	–	6×10^{-17}	COMET Phase-II [179]
BR $(\mu \to e)^{\mathrm{Al}}$	–	–	6×10^{-17}	Mu2e [181]
BR $(\mu \to e)^{\mathrm{Al}}$	–	–	3×10^{-18}	Mu2e II [180]
BR $(\mu \to e)^{\mathrm{Si}}$	–	–	2×10^{-14}	DeeMe [182]
BR $(\mu \to e)^{\mathrm{Ti}}$			$\sim 10^{-20} - 10^{-18}$	PRISM/PRIME [183, 184]
BR($\mu \to e\bar{e}e$)	$< 1.0 \times 10^{-12}$	SINDRUM [185]	$\sim 10^{-16}$	Mu3e [186]
BR($\tau \to 3\mu$)	$< 2.1 \times 10^{-8}$	Belle [187]	$\sim 10^{-9}$	Belle II [177]
BR($\tau \to 3e$)	$< 2.7 \times 10^{-8}$	Belle [187]	$\sim 10^{-9}$	Belle II [177]

Table 3.4 Experimental upper limits on various Leptonic flavour violation (LFV) processes.

The branching ratio of the radiative leptonic decays is given by,

$$\mathrm{BR}(\ell' \to \ell\gamma) = \frac{m_{\ell'}^5}{4\pi\Gamma_{\ell'}} \left(|C_T^L|^2 + |C_T^R|^2 \right). \tag{3.28}$$

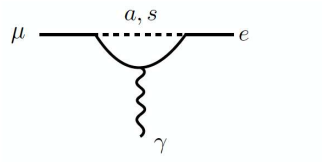

Fig. 3.8 Feynman diagram representing $\mu \to e\gamma$ decay.

The radiative leptonic decays receive the one-loop contribution, as shown in figure 3.8. The Wilson coefficients corresponding to the one-loop contribution read

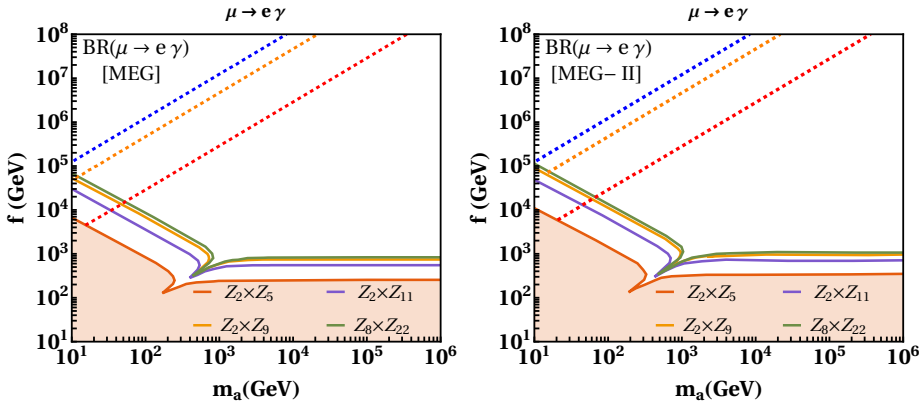

(a) (b)

Fig. 3.9 Bounds on the $f - m_a$ parameter space of the flavon of different $\mathscr{Z}_N \times \mathscr{Z}_M$ models by BR($\mu \to e\gamma$) for current as well as projected measurements from MEG and MEG-II experiments. The region above continuous curves represents the allowed parameter space for the corresponding $\mathscr{Z}_N \times \mathscr{Z}_M$ flavour symmetries in the soft symmetry-breaking scenario. The dashed lines show the allowed parameter space in the symmetry-conserving scenario. For both the scenario, $\lambda_\chi = 2$.

as [102],

$$C_T^L = (C_T^R)^* = \frac{e}{32\pi^2} \sum_{k=e,\mu,\tau} \left\{ \frac{1}{6} \left(y_{\ell k}^* y_{\ell' k} + \frac{m_\ell}{m_k} y_{k\ell}^* y_{k\ell'} \right) \left(\frac{1}{m_s^2} - \frac{1}{m_a^2} \right) \right.$$
$$\left. - y_{\ell k} y_{k\ell'} \frac{m_k}{m_{\ell'}} \left[\frac{1}{m_s^2} \left(\frac{3}{2} + \log \frac{m_{\ell'}^2}{m_s^2} \right) - \frac{1}{m_a^2} \left(\frac{3}{2} + \log \frac{m_{\ell'}^2}{m_a^2} \right) \right] \right\}. \tag{3.29}$$

The $\mu \to e\gamma$ decay impose the most stringent constraints on the parameter space of flavon of the $\mathscr{Z}_8 \times \mathscr{Z}_{22}$ and $\mathscr{Z}_2 \times \mathscr{Z}_9$ flavour symmetries in the soft symmetry-breaking scenario, as observed in figure 3.9a and 3.9b for the MEG and MEG-II experiments. This is followed by the $\mathscr{Z}_2 \times \mathscr{Z}_{11}$ flavour symmetry. For the symmetry-conserving case, the strongest bounds arise for the flavon of the $\mathscr{Z}_2 \times \mathscr{Z}_{11}$ flavour symmetry, followed by the flavon of the $\mathscr{Z}_2 \times \mathscr{Z}_9$ flavour symmetry.

3.2.2 $A\ \mu \to A\ e$ conversion

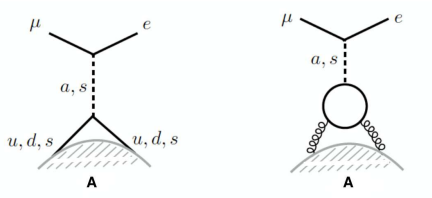

Fig. 3.10 Feynman diagram showing $A\ \mu \to A\ e$ conversion.

We write the following effective Lagrangian describing $A\ \mu \to A\ e$ conversion,

$$\mathscr{L}_{\text{eff}} = C_{qq}^{VL}\,\bar{e}\gamma^{\nu}P_L\mu\,\bar{q}\gamma_{\nu}q + m_{\mu}m_q C_{qq}^{SL}\bar{e}P_R\mu\,\bar{q}q + m_{\mu}\alpha_s C_{gg}^{L}\bar{e}P_R\mu\,G_{\rho\nu}G^{\rho\nu} + (R \leftrightarrow L), \tag{3.30}$$

Moreover, the dipole operators given in equation (3.27) provide additional contribution to $A\ \mu \to A\ e$ conversion. We show the Feynman diagram for $A\ \mu \to A\ e$ conversion in figure 3.10. The Wilson coefficients for the diagram on the left in figure 3.10 are given by [102],

$$\begin{aligned} C_{qq}^{SL} &= \left(\frac{1}{m_s^2} + \frac{1}{m_a^2}\right) y_{\mu e}^{*}\text{Re}(y_{qq})\,, \\ C_{qq}^{SR} &= \left(\frac{1}{m_s^2} - \frac{1}{m_a^2}\right) y_{e\mu}\text{Re}(y_{qq})\,. \end{aligned} \tag{3.31}$$

The nucleon-level Wilson coefficients which include the nuclear effects of quarks inside the nucleons as well as the contribution of the Feynman diagram on the right side of figure 3.10 can be written as,

$$\begin{aligned} \tilde{C}_p^{VL} &= \sum_{q=u,d} C_{qq}^{VL} f_{V_q}^{p}, \\ \tilde{C}_p^{SL} &= \sum_{q=u,d,s} C_{qq}^{SL} f_q^{p} - \sum_{Q=c,b,t} C_{QQ}^{SL} f_{\text{heavy}}^{p}\,, \end{aligned} \tag{3.32}$$

where the proton quark content is parameterized by the vector and scalar couplings $f^p_{V_q}, f^p_q$, and $f^p_{\text{heavy}} = 2/27\left(1 - f^p_u - f^p_d - f^p_s\right)$ [188]. For right-handed operators, analogous expressions can be obtained by replacing L with R, and for the neutron p is replaced by n. The contribution of the vector operators is much less than that of the scalar operators. Therefore, it can be ignored [102]. We use the numerical values of vector and scalar couplings given in references [189, 190], which are obtained after using the lattice average given in reference [191],

$$f^p_u = 0.0191, \quad f^n_u = 0.0171, \qquad f^p_d = 0.0363, \quad f^n_d = 0.0404, \qquad f^p_s = f^n_s = 0.043\,. \tag{3.33}$$

After including nuclear effects, the $A\ \mu \to A\ e$ conversion rate reads as [102],

$$\Gamma_{A\ \mu\to A\ e} = \frac{m^5_\mu}{4}\left|C^L_T D + 4\left[m_\mu m_p \tilde{C}^{SL}_p + \tilde{C}^{VL}_p V^p + (p \to n)\right]\right|^2 + L \to R, \tag{3.34}$$

where the dimensionless coefficients $D, S^{p,n}$, and $V^{p,n}$ are functions of the overlap integrals of the initial state muon and the final-state electron wave functions with the target nucleus. We use their numerical values given in table 3.5 [192].

Target	D	S^p	S^n	V^p	V^n	$\Gamma_{\text{capt}}[10^6\text{s}^{-1}]$
Au	0.189	0.0614	0.0918	0.0974	0.146	13.06
Al	0.0362	0.0155	0.0167	0.0161	0.0173	0.705
Si	0.0419	0.0179	0.0179	0.0187	0.0187	0.871
Ti	0.0864	0.0368	0.0435	0.0396	0.0468	2.59

Table 3.5 Numerical values of the dimensionless coefficients $D, S^{p,n}$, $V^{p,n}$ and the muon capture rate for different nuclei where Γ_{capt} denotes the muon capture rate.

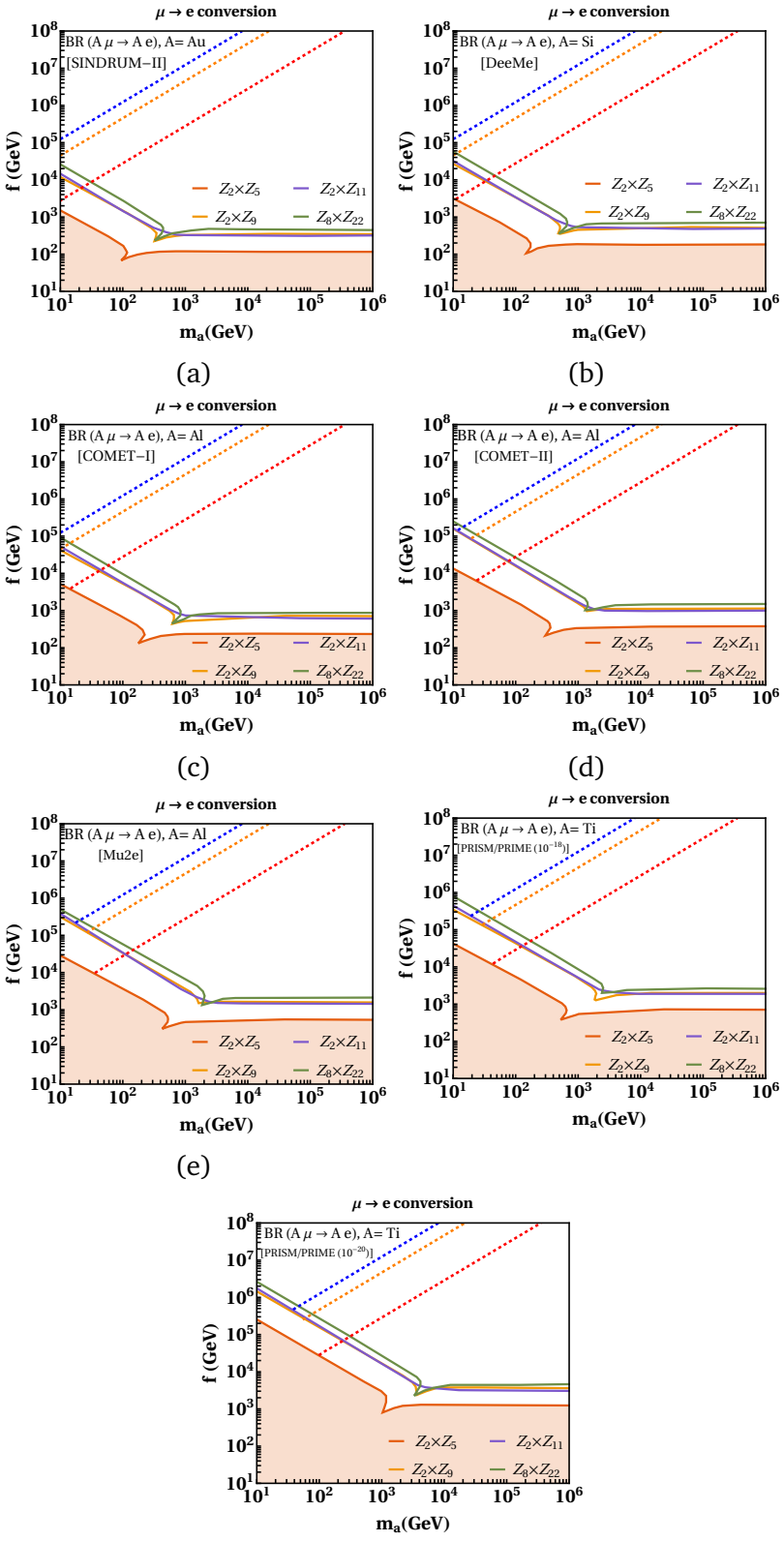

Fig. 3.11 Bounds on the $f - m_a$ parameter space of the flavon of different $\mathscr{Z}_N \times \mathscr{Z}_M$ symmetries by BR$(A\mu \to Ae)$ for the current as well as projected sensitivities of the experiments given in table 3.4. The coloured region represents the excluded parameter space by all four $\mathscr{Z}_N \times \mathscr{Z}_M$ symmetries in the soft symmetry-breaking scenario, while the dashed lines represent the allowed parameter space in the symmetry-conserving scenario.

The most stringent constraints from the A $\mu \to A$ e conversion rate on the parameter space of flavon of $\mathscr{Z}_N \times \mathscr{Z}_M$ flavour symmetries arise for the $\mathscr{Z}_8 \times \mathscr{Z}_{22}$ and $\mathscr{Z}_2 \times \mathscr{Z}_{9,11}$ flavour symmetries. The bounds from the future experiments are remarkably stronger than the existing limits. This can be seen in figure 3.11 for different ongoing and future experiments. This is followed by the $\mathscr{Z}_2 \times \mathscr{Z}_5$ flavour symmetries. In the symmetry-conserving scenario, the most stringent bounds are for the $\mathscr{Z}_2 \times \mathscr{Z}_{11}$ flavour symmetry, followed by the $\mathscr{Z}_2 \times \mathscr{Z}_{9,5}$ flavour symmetries.

3.2.3 $\mu \to 3e$ and $\tau \to 3\mu$ decays

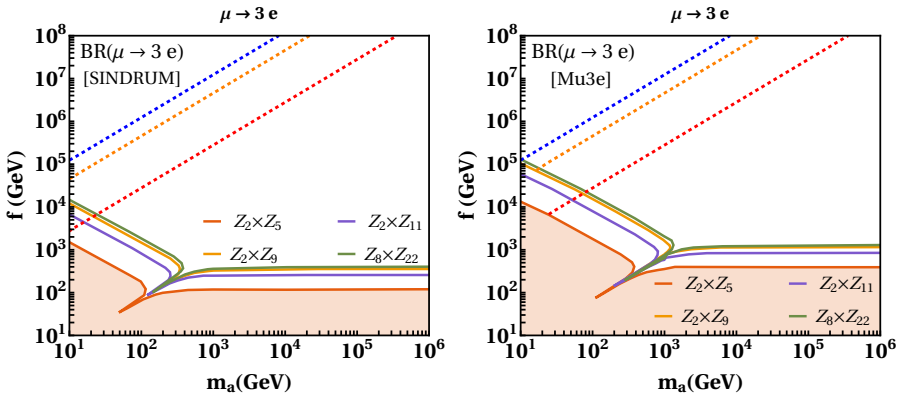

(a) (b)

Fig. 3.12 Bounds on the $f - m_a$ parameter space of the flavon of different $\mathscr{Z}_N \times \mathscr{Z}_M$ symmetries by BR$(\mu \to 3e)$ for sensitivities of the SINDRUM and Mu3e experiments. The coloured region represents the excluded parameter space by all four $\mathscr{Z}_N \times \mathscr{Z}_M$ symmetries in the soft symmetry-breaking scenario, while the dashed lines represent the allowed parameter space in the symmetry-conserving scenario.

The additional probes of the dipole operators given in equation (3.27) can emerge from the three body flavour violating leptonic decays $\mu \to 3e$ and $\tau \to 3\ell$ where $\ell = e, \mu$. The decay width of these decays is given by [102],

$$\Gamma(\ell' \to 3\ell) = \frac{\alpha m_\ell'^5}{12\pi^2} \left| log \frac{m_\ell'^2}{m_\ell^2} - \frac{11}{4} \right| \left(|C_T^L|^2 + |C_T^R|^2 \right). \tag{3.35}$$

where the tree-level contribution is negligible due to the strong chiral-suppression caused by the logarithmic enhancement of the dipole operators[102]. We ignore other contributions, such as Z-mediated penguin, due to their strong suppression [193].

The $\mu \to 3e$ decays places the most stringent bounds on the parameter space of flavon of the $\mathscr{Z}_8 \times \mathscr{Z}_{22}$ flavour symmetry for the soft symmetry-breaking case as shown in figure 3.12 for the SINDRUM and Mu3e experiments. The bounds on the flavour symmetry $\mathscr{Z}_2 \times \mathscr{Z}_9$ are almost similar to that of the $\mathscr{Z}_8 \times \mathscr{Z}_{22}$ flavour symmetry. This is followed by the $\mathscr{Z}_2 \times \mathscr{Z}_{11}$ flavour symmetry. For the symmetry-conserving scenario, the strongest bounds are for the $\mathscr{Z}_2 \times \mathscr{Z}_{11}$ flavour symmetry, followed by the $\mathscr{Z}_2 \times \mathscr{Z}_{9,5}$ flavour symmetries.

3.3 Summary of the flavour bounds

In figure 3.13, we present the summary of the most significant bounds on the parameter space of the flavon of different $\mathscr{Z}_{\rm N} \times \mathscr{Z}_{\rm M}$ flavour symmetries. We notice that in the soft symmetry-breaking scenario the most stringent bound for the $\mathscr{Z}_2 \times \mathscr{Z}_5$ flavour symmetry arise from the observable $|M_{12}^D|$, while for the $\mathscr{Z}_2 \times \mathscr{Z}_9$ and $\mathscr{Z}_8 \times \mathscr{Z}_{22}$ flavour symmetries, bounds from the observable C_{ε_K} are most stringent, and in the case of the $\mathscr{Z}_2 \times \mathscr{Z}_{11}$ the observable C_{B_d} in the phase-II of the LHCb places the strongest constraint. For the symmetry-conserving scenario, the most significant bounds for every $\mathscr{Z}_{\rm N} \times \mathscr{Z}_{\rm M}$ flavour symmetry are shown with the dashed straight-lines in figure 3.13.

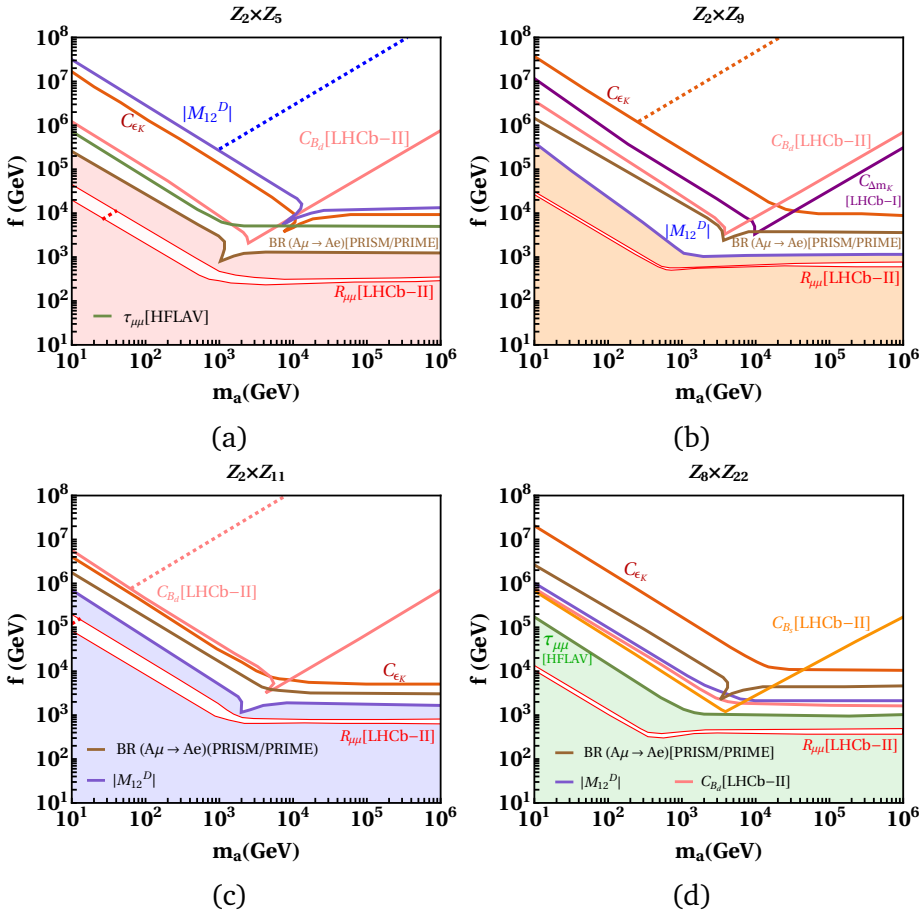

Fig. 3.13 Summary of the excluded parameter space constrained significantly by the quark and leptonic flavour observables for different $\mathscr{Z}_N \times \mathscr{Z}_M$ flavour symmetries are shown with the coloured region in the soft symmetry-breaking scenario. The dashed line represents the allowed parameter space, which is most stringently constrained by the corresponding flavour observable in the symmetry-conserving scenario, except for the $\mathscr{Z}_8 \times \mathscr{Z}_{22}$ flavour symmetry.